Journal of Molecular Catalysis B: Enzymatic 75 (2012) 60–67

Contents lists available at SciVerse ScienceDirect

Journal of Molecular Catalysis B: Enzymatic

journal homepage: www.elsevier.com/locate/molcatb

Carbonic anhydrase conjugated to nanosilver immobilized onto mesoporous SBA-15 for sequestration of CO_2

Mari Vinoba [a], Margandan Bhagiyalakshmi [b], Soon Kwan Jeong [a,*], Yeo Il Yoon [a], Sung Chan Nam [a]

[a] Korea Institute of Energy Research, Daejeon 305-343, Republic of Korea
[b] Department of Chemistry, University College of Engineering Arni, Anna University, Chennai 600 025, India

ARTICLE INFO

Article history:
Received 12 July 2011
Received in revised form 9 November 2011
Accepted 9 November 2011
Available online 18 November 2011

Keywords:
Carbonic anhydrase
SBA-15
Silver nanoparticles
Immobilization
CO_2 capture
Sequestration

ABSTRACT

Human carbonic anhydrase (HCA) was conjugated via electrostatic interactions onto silver nanoparticles confined to amine-functionalized mesoporous SBA-15. Three amine compounds were tested for their effectiveness in immobilizing silver nanoparticles: tris(2-aminoethyl)amine (TAEA), tetraethylenepentamine (TEPA), and octa(aminophenyl)silsesquioxane (OAPS). The enzymatic activities of the free and nanosilver conjugated HCA were assessed by measuring the hydrolysis of p-nitrophenylacetate (p-NPA) and the hydration of CO_2, which was sequestered as $CaCO_3$. The CO_2 conversion efficiency was calculated using ion chromatography methods, and $CaCO_3$ formation was observed by polarized light microscopy. Precipitated $CaCO_3$ was characterized by XRD and FE-SEM. After 30 cycles, the silver conjugated HCA showed the highest operational stability, and the CO_2 capture efficiency was ~25 fold higher than that of free HCA. Storage stability studies suggested that conjugated HCA retained nearly 87% of its activity after 30 days. The results demonstrated that immobilized HCA was reusable and stable under storage conditions. Thus, this nanobiocatalyst is a suitable candidate for the capture and sequestration of CO_2.

1. Introduction

The atmospheric concentrations of anthropic CO_2 emissions are predicted to rise from 29.7 Gt to about 33.8 Gt in 2020 and 42.4 Gt in 2035 due to the use of crude oil, coal, and natural gas, which contribute 40%, 40% and 20%, respectively [1]. Strategies to reduce CO_2 emissions involve two steps: the separation of CO_2 from other gases, and the storage of captured CO_2 in a liquid or solid condensed form. Researchers have studied the problem of CO_2 emissions, but no panacea is yet available. CO_2 capture and separation technologies frequently involve amine solvents [2], metal oxides [3], nickel complexes [4], surface-modified silicas [5], zeolites [6], and metal-organic frameworks [7], and each process has its associated pros. and cons. One of the most promising methods proposed thus far is biological CO_2 sequestration, in which CO_2 is sequestered as calcium carbonate by carbonic anhydrase (CA). CA is a major zinc-based metalloenzyme that catalyzes the conversion of CO_2 to bicarbonate or vice versa [8]. Bicarbonate ions can precipitate as insoluble $CaCO_3$ by reacting with soluble calcium ions. The use of soluble CA is limited because of the short lifetime and difficulties associated with its reuse. Several methods have been proposed to improve the catalytic stability of the enzyme, such as enzyme immobilization or modification, or medium engineering. Immobilization of the enzyme onto a solid support is the best approach for the sequestering applications contemplated in this context. Recently, enzymes have been immobilized over nanostructure materials via electrostatic interactions and physicochemical forces [9]. The immobilization of enzymes yields several advantages over their solution counterparts including enhanced temperature and storage stability of the biocatalyst and ease of separation from the reaction medium, which enables reuse. Nanotechnology has achieved several advances in engineering biocompatible surfaces, and such developments play a vital role in the immobilization of biomolecules [10,11] for environmental [12], biosensor, and medicine applications [13,14]. Many metals, such as silver [15–19], gold [20–22], zirconium [23], and magnetic nanoparticles [24,25], have been employed in the synthesis of metal nanoparticle–enzyme conjugate materials. Reports of such uses have focused on enzyme molecules bound tightly to the metal nanoparticles, and studies have showed that such conjugates retain significant biocatalytic activity. The immobilization of carbonic anhydrase has been achieved via a number of approaches with the goal of improving the enzymatic activity of the immobilized species [26–31]. In the present study, human carbonic anhydrase (HCA) was immobilized onto Ag nanoparticles bound within the channels amine-functionalized SBA-15 which is extension of an earlier report [32]. Here, amine functionalized SBA-15 prevents the agglomeration of nanoparticles and provides a good distribution of stabilized nanoparticles over the surface. Three amino compounds, tris(2-aminoethyl)amine (TAEA), tetraethylene pentamine (TEPA),

* Corresponding author. Tel.: +82 42 860 3623; fax: +82 42 860 3134.
E-mail address: jeongsk@kier.re.kr (S.K. Jeong).

1381-1177/$ – see front matter © 2011 Elsevier B.V. All rights reserved.
doi:10.1016/j.molcatb.2011.11.010

and octa(aminophenyl)silsesquioxane) (OAPS), which contain five or eight amine groups, were grafted onto the SBA-15 surfaces for this purpose [33–35]. The organic amine compounds TEPA and TAEA are small, whereas OAPS is a derivative of polyhedral oligomeric silsesquioxanes (POSS) and has a molecular diameter of 1.5 nm [36]. OAPS includes eight amine groups on each edge of a cubic silicon cage structure. The immobilization of these amine compounds onto SBA-15 preserved the mesoporous characteristics of SBA-15 substrate.

Herein, large-pore short-channel mesoporous SBA-15 was synthesized using TEOS and P123 (as silica source and template) and grafted with TAEA/TEPA/OAPS SBA-15 for further functionalized with silver nanoparticles for the immobilization of HCA. HCA bound strongly to the silver nanoparticle surfaces and showed excellent biocatalytic activity, as demonstrated by the hydrolysis of p-nitrophenylacetate (p-NPA). Furthermore, CO_2 hydration and sequestration to $CaCO_3$ were studied over immobilized HCA on silver nanoparticles confined to TAEA/TEPA/OAPS-functionalized mesoporous SBA-15. The activities of the immobilized HCA toward hydration and sequestration of CO_2, reusability, CO_2 conversion efficiency, and quantity of $CaCO_3$ generated, were measured using ion chromatography techniques. $CaCO_3$ formation was observed by polarized light microscopy.

2. Experimental

2.1. Materials

Human carbonic anhydrase (HCA), tetraethyl orthosilicate (TEOS), P123 triblock copolymer (MW 5800), trimethyl benzene (TMB), tris (2-aminoethyl) amine (TAEA), tetraethylene pentamine (TEPA), tetrahydrofuran (THF), sodium borohydride ($NaBH_4$), 2-amino 2-(hydroxymethyl)-1,3-propanediol (Tris base), silver nitrate, p-nitrophenol (p-NP), p-nitrophenyl acetate (p-NPA), acetonitrile, calcium chloride ($CaCl_2{\cdot}6H_2O$) and the Bradford reagent were all purchased from Sigma Aldrich and Octa(aminophenyl)silsesquioxane (OAPS) was obtained from hybrid polymer (AM0280) used without further purification. All solutions were prepared with deionized water.

2.2. Immobilization of nanosilver on amine-functionalized SBA-15

Short-channel SBA-15 was synthesized as described in the literature [37,38], with modifications. Typically, 4 g P123 were dissolved in 150 mL 1.6 M HCl at 40 °C, and the slurry was stirred until complete dissolution was achieved. After the addition of a swilling agent, 0.3 g TMB, the reaction was stirred for 2 h, and a silica precursor, 9.2 mL TEOS, was then added. The mixture was stirred at 40 °C for 10 min, further allowed for 24 h at 40 °C under static conditions, then aged at 120 °C for 24 h. The mixture was cooled and filtered. The white powder was allowed to dry in air under vacuum for 24 h, and then was calcined in air at 550 °C for 6 h with a heating rate of 1 °C/min. The final product was denoted SBA-15. A quantity of 50 mM CPTMS was added to 1 g SBA-15 dispersed in 70 ml dry toluene with stirring. The reaction was refluxed for 24 h, and the final product was filtered, washed with toluene then alcohol, and dried under vacuum at 70 °C for 8 h. The product was denoted CPTMS/SBA-15 (Scheme 1) Step 1. The amine compounds (TAEA/TEPA/OAPS) were subsequently grafted onto 1 g CPTMS/SBA-15 using a procedure adopted for CPTMS grafting [33–35]. OAPS grafting was performed in THF (Scheme 1) Step 2. Silver nanoparticles were immobilized on functionalized SBA-15 as described [32,33]. The products were denoted Ag/TAEA/SBA-15, Ag/TEPA/SBA-15, and Ag/OAPS/SBA-15 (Scheme 1) Step 3.

2.3. Formation of the HCA–nanosilver/SBA-15 bioconjugated product

HCA was immobilized onto Ag/TAEA/SBA-15, Ag/TEPA/SBA-15, and Ag/OAPS/SBA-15 as described previously [32]. Immobilized materials were denoted HAg-1, HAg-2, and HAg-3, respectively

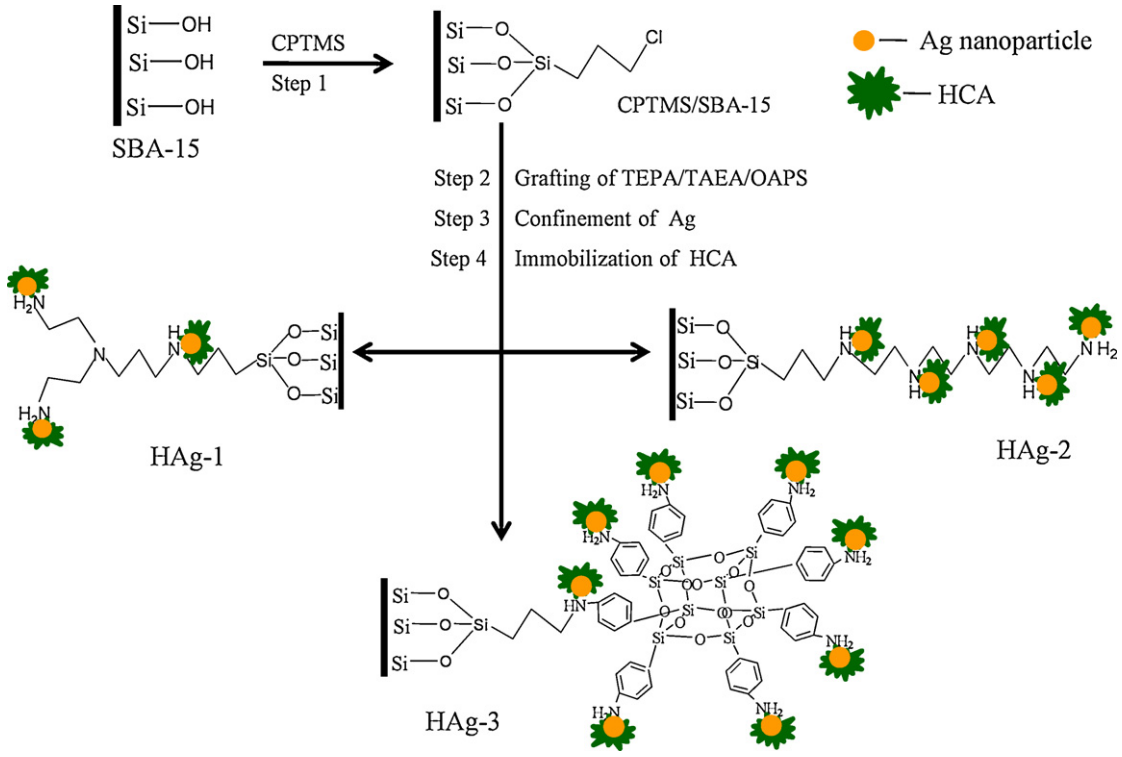

Scheme 1. Synthesis of nanosilver confined mesoporous SBA-15 and followed by HCA immobilization.

(Scheme 1) Step 4. The quantities of immobilized and unbounded HCA were calculated by the Bradford method. The biocatalytic activity of HAg-1, HAg-2, and HAg-3 were estimated using p-NPA as described [32].

2.4. Hydration and carbonization of CO_2 over free HCA, HAg-1, HAg-2, and HAg-3

Hydration of CO_2 by a fixed quantity of 5 mg HCA (HAg-1, HAg-2, or HAg-3) was tested by dispersing the HCA-bearing material in 25 mL of a 1.0 M Tris–HCl buffer solution (pH 6.4), followed by addition of 100 mL of a saturated CO_2 solution (0.149 wt%) [39]. Hydration of CO_2 was determined to be complete when no further changes in pH were observed. HAg-1, HAg-2, and HAg-3 was recovered after centrifugation of hydrated CO_2 solution on refrigerated centrifuge (Hanil Combi-514R, at 12,000 rpm for 5 min) for subsequent cycles. The recovered materials were treated with 25 mL of a calcium ion solution (360 mg Ca^{2+}, 1.5 M Tris base) at pH 10.0 with stirring for 1 h. $CaCO_3$ crystal formation was observed by polarized light microscopy. The solubility product of $CaCO_3$ [40] was used to quantify the precipitated carbonate by indirect methods: ion chromatography (IC) coupled with a conductivity detector. After 1 h, the precipitated $CaCO_3$ was filtered (0.22 μm), and calcium ions in solution were quantified by running the filtrate over a cationic column (silica gel with carboxyl groups). Precipitated $CaCO_3$ was dried at 60 °C and characterized by XRD. For comparison, hydration of CO_2 and precipitated $CaCO_3$ was performed in the presence of 5 mg free HCA.

2.5. Characterization of materials

X-ray diffraction patterns (XRD) were recorded using a Rigaku Miniflex diffractometer with Cu-Kα radiation (λ = 0.154 nm). The diffraction data were recorded over the 2θ range 0.5–80° at a 0.02° step size with 1 s step time. Nitrogen adsorption–desorption isotherms were measured on a Micromeritics ASAP 2010 volumetric adsorption analyzer. The Brunauer–Emmett–Teller (BET) specific surface areas (S_{BET}) were determined using the BET equation; the pore size distribution was estimated using the Barrett–Joyner–Halenda (BJH) method. ^{13}C CP MAS NMR spectrum was recorded on a Varian Inova 600 MHz spectrometer at 100.6 and 79.4 MHz with a sample spinning frequency of 5 kHz. FE-SEM images were captured on a Hitachi S-4700. High Resolution Transmission Electron Microscopy (HR-TEM) and Energy dispersive X-ray diffraction spectroscopic (EDS) analysis were performed on a JEOL-2000EX electron microscope operating at an accelerating voltage of 120 kV. Zeta potential testing was carried out using an Otasuka electronics zeta potential analyzer (ELS-8000) at 25 °C in pH 6.4 phosphate buffer solution. Calcium ions were quantified by ion chromatography (IC) using Metrosep C2-150 cationic column coupled with a conductivity detector (Metrohm 801 Compact IC pro). Data were collected using the magic Net 2.1 software. The eluent contained a mixture of tartaric acid/dipicolinic acid (4 mmol/0.75 mmol). $CaCO_3$ crystal formation was observed by polarized light microscopy, and images were captured using an Olympus BX51M with a megapixel firewire camera (PL-A662).

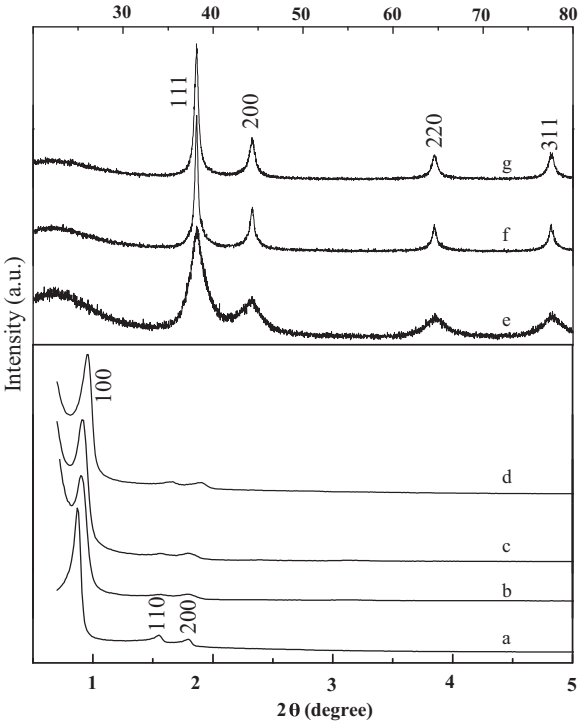

Fig. 1. XRD patterns of SBA-15 (a), Ag/TAEA/SBA-15 (b and e), Ag/TEPA/SBA-15 (c and f) and Ag/OAPS/SBA-15 (d and g).

3. Results and discussion

3.1. Physicochemical characterization of functionalized SBA-15

XRD patterns of the SBA-15, Ag/TAEA/SBA-15, Ag/TEPA/SBA-15, and Ag/OAPS/SBA-15 are shown in (Fig. 1). The low-angle XRD patterns of Ag/TAEA/SBA-15, Ag/TEPA/SBA-15, and Ag/OAPS/SBA-15 showed peaks at 2θ = 0.8°, 1.5°, and 1.8°, which revealed the presence of (1 0 0), (1 1 0), and (2 0 0) planes due to the well-ordered hexagonal mesophase (Fig. 1a and d). The intensity of these patterns was slightly less than the intensity of the corresponding patterns from the parent SBA-15. The XRD pattern intensity is a function of the scattering contrast between the silica walls and the pore channel, and is possibly sensitive to pore filling by the CPTMS grafting, TAEA/TEPA/OAPS and Ag nanoparticle immobilization [33]. The wide angle XRD patterns of Ag/TAEA/SBA-15, Ag/TEPA/SBA-15, and Ag/OAPS/SBA-15 confirmed the presence of silver nanoparticles at 2θ = 38°, 44°, 65°, 44.1°, and 78° corresponding to the faces (1 1 1), (2 0 0), (2 2 0), and (3 1 1), respectively (Fig. 1e and g). The surface areas of the amine-grafted SBA-15 materials were evaluated by the BET method, and the pore sizes were measured using the BJH method. The physicochemical properties of the materials are summarized in (Table 1). The nitrogen adsorption/desorption of pristine SBA-15 displayed a type IV isotherm with a well-defined hysteresis loop. Successive functionalization of CPTMS, TAEA/TEPA/OAPS, and Ag nanoparticles on the SBA-15 surfaces decreased the specific surface area, pore volume, and pore diameter. Such significant

Table 1
Physicochemical characterization of SBA-15.

Material	SBA-15	Ag/TAEA/SBA-15	Ag/TEPA/SBA-15	Ag/OAPS/SBA-15
Surface area (m^2/g)	712	195	163	138
Pore diameter (nm)	13.5	6.73	6.28	5.87
Mean pore volume (cm^3/g)	1.34	0.75	0.63	0.56
Zeta potential (mV)	–	−8.23	−14.95	−19.60

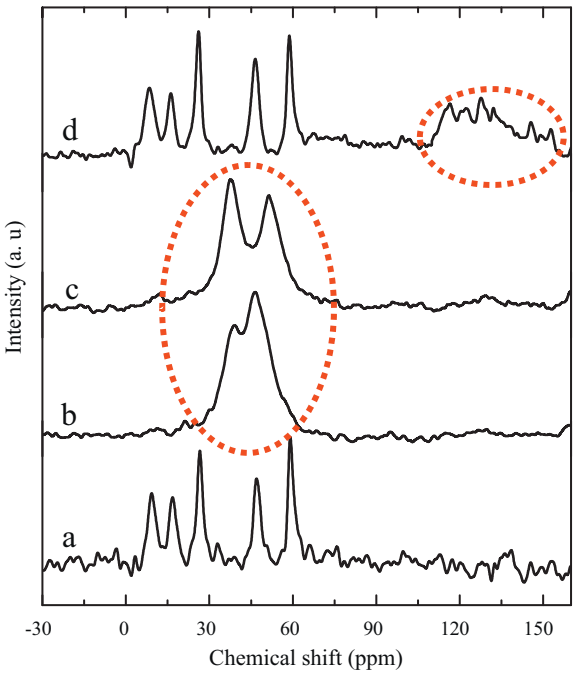

Fig. 2. ^{13}C CP MAS NMR analysis of SBA-15 (a), CPTMS/SBA-15 (b), TEPA/SBA-15 (c), TAEA/SBA-15 (d) and OAPS/SBA-15 (e).

decreases in the textural properties of the porous materials upon grafting have been reported previously [32,33].

The ^{13}C CP MAS NMR of CPTMS/SBA-15 displayed three peaks corresponding to the carbon atoms (Si–CH_2, –CH_2, and Cl–CH_2) of the chloropropyl moiety at 10.2, 26.8, and 49.3 ppm, respectively (Fig. 2a). This confirmed the successful grafting of chloropropyl moieties. The presence of peaks at 18 and 62 ppm indicated the presence of residual ethoxy groups [41]. Broad peaks at 60–20 ppm were observed due to the presence of TEPA or TAEA grafted via a chloropropyl moiety (Fig. 2b and c). OAPS grafting was confirmed by the presence of new peaks at 160–110 ppm, attributed to ^{13}C resonances of the carbon atoms on the benzene rings (Fig. 2d) [42].

HR TEM images of the parent SBA-15 showed hexagonally arranged mesopores. Dark spots in the images of Ag/TEPA/SBA-15, Ag/TEPA/SBA-15, and Ag/OAPS/SBA-15 indicated stabilization of silver nanoparticles inside the hexagonal mesopores of TAEA/SBA-15, TEPA/SBA-15, and OAPS/SBA-15 (Fig. 3). The silver nanoparticles were formed through the reduction of Ag^+ ions by $NaBH_4$, which had been introduced by impregnation to the inside pore channels of the amine-grafted SBA-15. The TEM images showed that Ag/OAPS/SBA-15 presented more dark spots, indicating the more number of silver nanoparticles, than Ag/TEPA/SBA-15 or Ag/TAEA/SBA-15 due to number of amine groups. Silver nanoparticles were immobilized by amine via electrostatic interactions [43]. The silver nanoparticle sizes ranged from 2 to 3 nm. The silver nanoparticles were confirmed by EDS spectrum of the Ag/TAEA/SBA-15, Ag/TEPA/SBA-15, and Ag/OAPS/SBA-15 materials (Figure not shown).

The surfaces of Ag/TAEA/SBA-15, Ag/TEPA/SBA-15, and Ag/OAPS/SBA-15 at pH 6.4 were negatively charged, as determined by zeta potential measurements, shown in (Table 1). The p*I* of HCA is 6.6, and HCA is positively charged at pH 6.4 (+3.81 mV) [32,44]. The parent SBA-15 surface is generally covered with silanol groups, which form a hydrophilic surface in aqueous media. The functionalization of SBA-15 silica surfaces, followed by Ag nanoparticle immobilization, transformed the surface properties from hydrophilic to hydrophobic. The shape of the HCA molecule is an ellipsoid of size ~4 nm [45]. From the BET results, the pore size of the Ag/TAEA/SBA-15, Ag/TEPA/SBA-15, Ag/OAPS/SBA-15 were 6.73, 6.28 and 5.87 nm respectively (Table 1), hence, Ag-confined

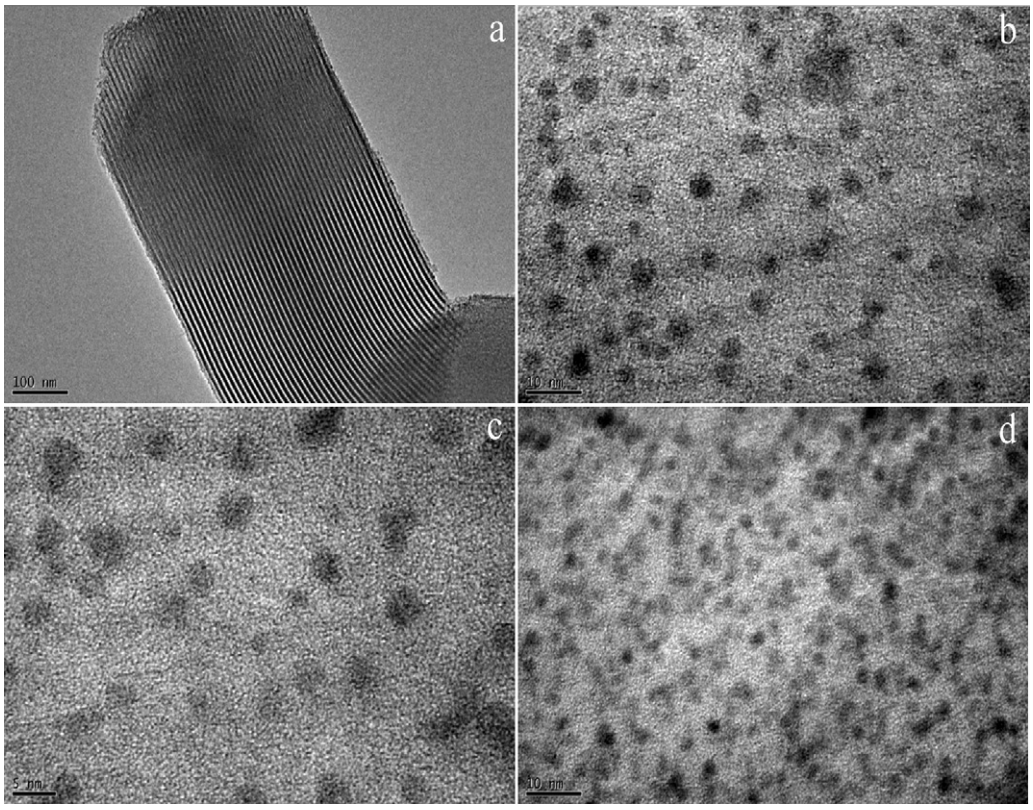

Fig. 3. HR-TEM images of SBA-15 (a), Ag/TEPA/SBA-15 (b), Ag/TAEA/SBA-15 (c) and Ag/OAPS/SBA-15 (d).

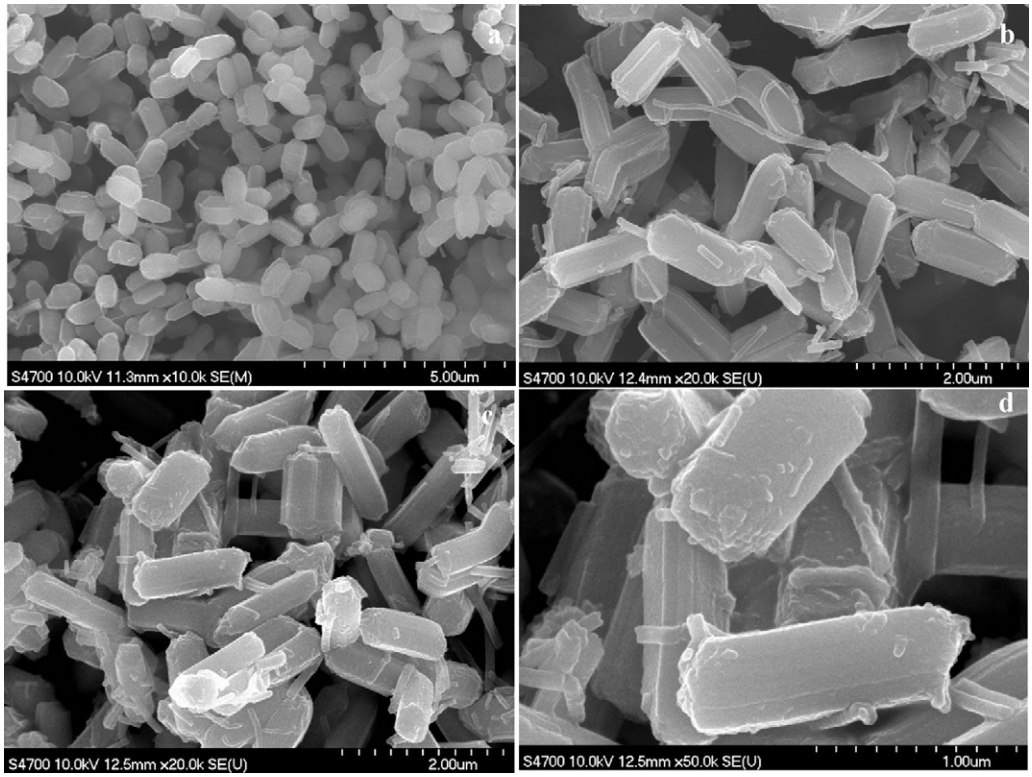

Fig. 4. FE-SEM images of SBA-15 (a), HAg-1 (b), HAg-2 (c) and HAg-3 (d).

SBA-15 possess large space to accommodate HCA. Furthermore, the enzyme–surface interactions were strongly affected by the electric charges and charge densities on both the HCA and the Ag-confined SBA-15. It has been previously shown [32] that the stability of an enzyme in harsh environments may be enhanced by conjugating the enzyme to a metal confined within SBA-15, as measured using the Bradford method [46]. HCA loading on the Ag/TAEA/SBA-15, Ag/TEPA/SBA-15, and Ag/OAPS/SBA-15 substrates was 226, 283, and 307 mg/g, respectively. The high level of HCA loading on the Ag/OAPS/SBA-15 substrate was achieved because the Ag nanoparticles were well-dispersed over the OAPS/SBA-15 surface, and bioconjugation between the Ag nanoparticles and HCA was efficient. The surface morphologies of the parent SBA-15, HAg-1, HAg-2, and HAg-3 materials displayed hexagonal rod structures, as captured by FE-SEM analysis (Fig. 4). The hexagonal structure was preserved, even after enzyme immobilization.

3.2. Enzymatic activity of free HCA, HAg-1, HAg-2, and HAg-3

The conversion mechanism of CO_2 to bicarbonate by HCA involves nucleophilic attack of Zn^{2+}-bound OH^- on the carbon of CO_2, internal proton transfer of Zn^{2+}-bound HCO_3^-, binding of water to Zn^{2+}, and ionization of Zn-bound water to facilitate the release HCO_3^-. Nucleophilic attack of Zn^{2+}-bound OH^- on CO_2 leaves a proton on a Zn^{2+}-bound oxygen, which could promote the reverse reaction, in which HCO_3^- can bind via an unprotonated oxygen to Zn^{2+}[8]. Bicarbonate ions are easily converted to carbonate ions at high pH, and, in the presence of Ca^{2+} cations, the carbonate ions are readily precipitated in the form of calcium carbonate.

Each molecule of CA can catalyze the hydration of 1.4×10^6 CO_2 molecules within 1 s, the local pH can vary dramatically and large uncertainties in the conversion rate would be expected [47]. Therefore, as reported previously [32], the biocatalytic activities of free HCA, and HAg-1, HAg-2, and HAg-3 was initially determined by the hydrolysis of p-NPA. The k_{cat}/k_m values of free, HAg-1, HAg-2, and HAg-3 were found to be 1660, 1580, 1590, 1640 $M^{-1}s^{-1}$, respectively (Table 2). Among HAg-1, HAg-2, and HAg-3, the latter produced the highest HCA loading and k_{cat}/k_m for the hydrolysis of p-NPA. The immobilization of enzyme molecules on the well-distributed Ag nanoparticles on the edges of the cubic OAPS moieties provided the best biocatalytic activity. Furthermore, the activity of free and immobilized HCA was also investigated for hydration of CO_2 and its precipitation to $CaCO_3$. HCA is stable

Table 2
Profile of free and immobilized HCA.

Parameters	Unit	Free HCA	HAg-1	HAg-2	HAg-3
k_{cat}/k_m[a]	$M^{-1}s^{-1}$	1660	1580	1590	1640
$CaCO_3$[b]	mg	290	280	280	280
Total amount of $CaCO_3$[c]	mg	–	7260	7590	7810
Efficiency (Free HCA/HAg)[c]	fold	1[b]	25	26	27

[a] p-NPA hydrolysis.
[b] Single cycle.
[c] After 30 cycles (Fig. 5b).

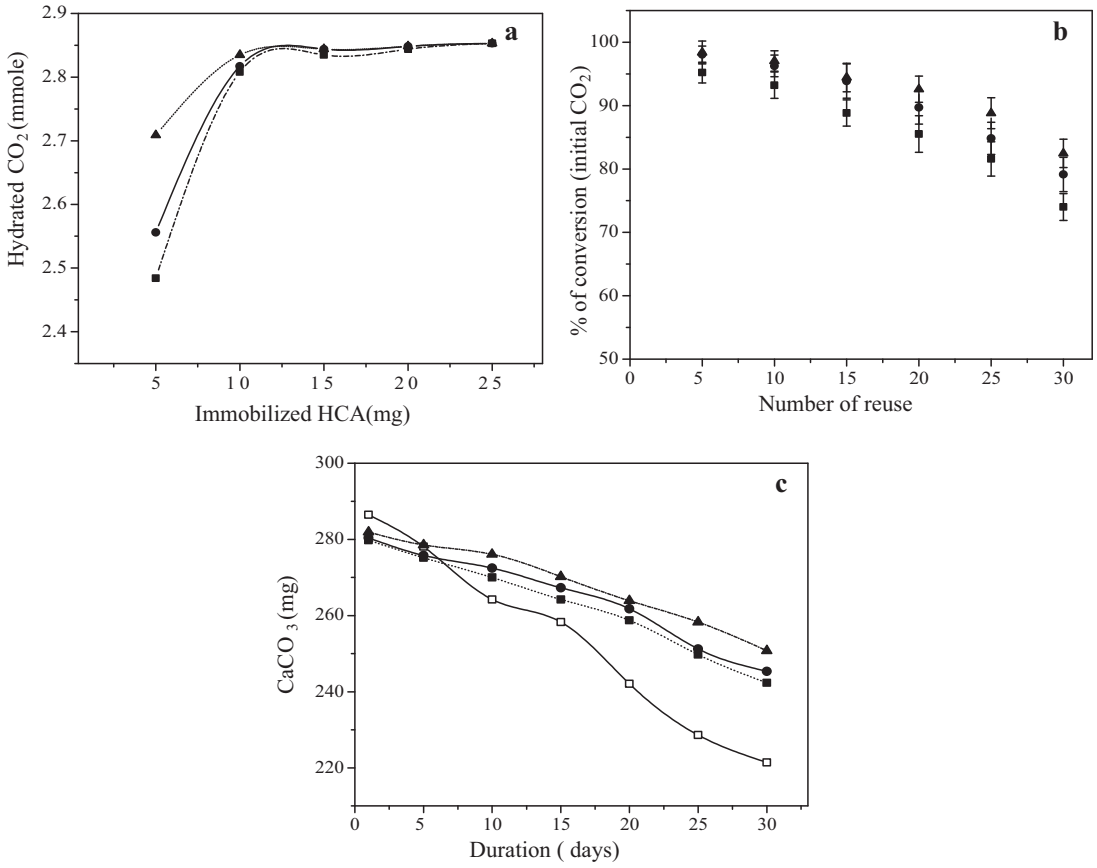

Fig. 5. Performance of free HCA (□), HAg-1(■), HAg-2(●) and HAg-3(▲)on: (a) optimization for CO_2 hydration, (b) effect of reusability for CO_2 conversion, (c) effect of storage stability for $CaCO_3$ precipitation.

and active at all pH between 5.8 and 8.8. At pH values below 5.8 the enzyme loses its activity over a period of time [48]. Therefore, activity of HAg-1, HAg-2, and HAg-3, for the hydration of CO_2 was investigated in a 0.5 M buffer solution (Tris–HCl, pH 6.4) and the results are in similar trend with that of p-NPA hydrolysis (Table 2).

Sequestration of CO_2 was conducted after hydration of CO_2 at pH 10.0 at 25 °C. $CaCO_3$ was quantified using indirect methods, in which calcium ions were measured by ion chromatography (IC) of the filtrate solution. The CO_2 conversion efficiency and $CaCO_3$ precipitation were calculated. In the IC method, the quantity of $CaCO_3$ measured was higher than the quantity of precipitated $CaCO_3$ collected due to losses associated with filtration and recovery. The enzyme concentration was optimized for the hydration and sequestration of CO_2. The extent of CO_2 hydration increased linearly with the amount of HAg-1, HAg-2, and HAg-3 support present (Fig. 5a). The hydrated CO_2 solution was treated with Ca^{2+} ions for 60 min. At an HCA concentration of 5 mg, the concentration of free Ca^{2+} ion in the reaction medium did not change. This suggests that a maximum conversion has reached with 5 mg of HCA, and higher amounts of HCA did not produce additional increases in the conversion rate. The gram equivalent of CO_2 sequestration was calculated according to the efficiency of converting Ca^{2+} to $CaCO_3$.

(Fig. 5b) shows 30 cycles of CO_2 hydration activity for the HAg-1, HAg-2, and HAg-3 substrates. The substrates were washed with 50 mM Tris–HCl buffer (pH 6.4) between each cycle and separated by centrifugation. After hydration and treatment with Ca^{2+} ions, carbonic acid was precipitated as $CaCO_3$ at pH 10, and unreacted Ca^{2+} ions were quantified by IC. The levels of unreacted Ca^{2+} were measured, and the CO_2 to CO_3^{2-} conversion efficiency relative to the initial CO_2 levels was calculated. The quantities of $CaCO_3$ precipitated by the same amount of enzyme concentration (5 mg) in free HCA, HAg-1, HAg-2, and HAg-3 at end of first cycle were given in (Table 2). The HAg-3 substrate retained 84% of its initial activity after 30 cycles, whereas the relative activities of HAg-2 and HAg-1 decreased to 19% and 33%, respectively. The high relative activities of HAg-3, HAg-2, and HAg-1 were due to the high electronegativity of the Ag/OAPS/SBA-15, Ag/TEPA/SBA-15, and Ag/TAEA/SBA-15 templates, which interacted strongly with HCA to yield a stable bioconjugated material. Although free HCA yielded an equal quantity of $CaCO_3$ during its first catalytic cycle, its reuse required considerable efforts. Thus, at the end of 30 cycles of CO_2 hydration and its precipitation, the total amount of $CaCO_3$ formation for HAg-1, HAg-2, and HAg-3 (∼5 mg of HCA was immobilized on supports) were 7260, 7590 and 7810 mg, respectively (Table 2), whereas with same amount (5 mg) of free enzyme, 290 mg of $CaCO_3$ was produced in one cycle and, no further precipitation is possible as HCA could not be recovered and reused. Therefore, from the amount of $CaCO_3$ precipitated over free and immobilized HCA, it was calculated that activity of HAg-1, HAg-2, and HAg-3 were 25, 26, and 27 –fold higher than the activity of the free HCA, respectively (Table 2). Thus, the above materials proved to be reusable sorbents, which is an essential requirement for industrial-scale biocatalysts designed to capture CO_2.

Fig. 5c shows the storage stability in a Tris–HCl buffer (50 mM, pH 6.4) of free HCA, HAg-1, HAg-2, and HAg-3 at 25 °C. The activities of the stored immobilized HCA were analyzed over 30 days at 5 days intervals for the hydration and sequestration of CO_2. The quantity of $CaCO_3$ and residual activities of free HCA, HAg-3, HAg-2, and HAg-1 were 221.4, 250.78, 245.36, and 242.35 mg, and 77%, 89%, 87.5%, and 86.5%, respectively after 30 days. The strong metal–protein

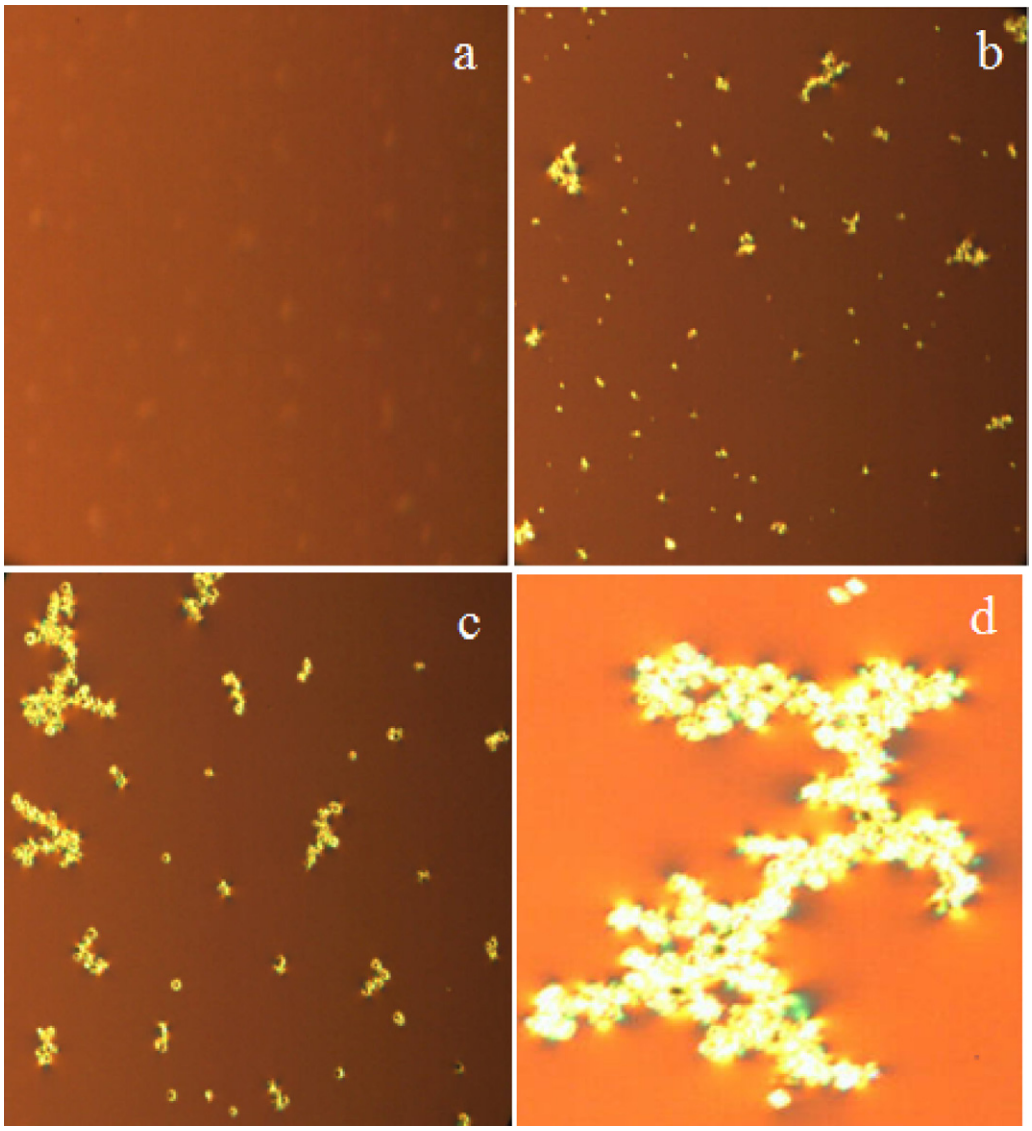

Fig. 6. Polarized light microscopy images of $CaCO_3$ precipitate, 1 min (a), 15 min (b), 30 min (c) and 60 min (d) obtained after nucleation.

interactions between HCA and Ag/OAPS/SBA-15, Ag/TAEA/SBA-15, and Ag/TEPA/SBA-15, contributed to the retention of its activity during long-term storage.

The formation of two $CaCO_3$ solid phases, calcite and vaterite, was studied as a function of time. A combination of vaterite and calcite phases was observed after 30 min reaction time, and these phases have been converted to a pure calcite phase after 60 min reaction time. Changes in the binding strength at pH 10.0 gives provided a favorable environment for the structural reformation and nucleation of different $CaCO_3$ species, which later transformed into the particular crystalline polymorphs. The nucleation of $CaCO_3$ was observed by polarized light microscopy over time (Fig. 6). Nucleation proceeded as follows: carbonate ions reacted with Ca^{2+} to form metastable $CaCO_3$ clusters during the pre-nucleation stage (Fig. 6a). The pre-nucleation stage (at 1 min) indicated the binding behavior of Ca^{2+}, which depended on the CO_3^{2-} concentration. Once nucleation began, the free Ca^{2+} ion concentration in solution decreased, and the growing clusters formed amorphous $CaCO_3$. In the post-nucleation stage, Ca^{2+} binding to CO_3^{2-} ions increased, and a mixture of vaterite and calcite phases formed at 15–30 min (Fig. 6b and c). At 60 min, calcite $CaCO_3$ formation was observed (Fig. 6d). The unbound Ca^{2+} ions in the clusters were quantified by IC methods. The polymorphic transformation from vaterite to calcite at 60 min was confirmed by XRD, discussed below.

XRD analysis of the $CaCO_3$ precipitate formed at pH 10.0 for different reaction times indicated formation of a pure calcite phase at 60 min and a mixture of vaterite and calcite at 30 min over HAg-3 (Fig. 7A). Diffraction peaks were observed at $2\theta = 25.04^\circ$, 27.16°, 32.8°, 44.1°, and 49.9°, corresponding to the vaterite crystal faces (1 0 0), (1 0 1), (1 0 2), (1 1 0), and (1 0 4), respectively. After 60 min, a pure calcite phase was observed due to phase reformation from vaterite. Diffraction peaks were observed at $2\theta = 29.5^\circ$, 36.1°, 39.5°, and 43.3°, corresponding to the calcite crystal faces (1 0 4), (1 1 0), (1 1 3), and (2 0 2), respectively (Fig. 7B) [49–51]. The morphologies of the vaterite and calcite particles obtained after 30 min over HAg-3 were determined by FE-SEM, as shown in (Fig. 7a). At 60 min, the rapid crystallization process converted all vaterite phase $CaCO_3$ to the calcite phase (Fig. 7b). Both $CaCO_3$ morphologies were hexagonal in structure, but vaterite was more complex with a packing that led to the growth of aggregates. On the other hand, the calcite crystals exhibited well-defined faceted rhombohedral characteristics at pH 10.0. The vaterite particles were porous, whereas the thin planar calcite crystals were not porous grew on the external

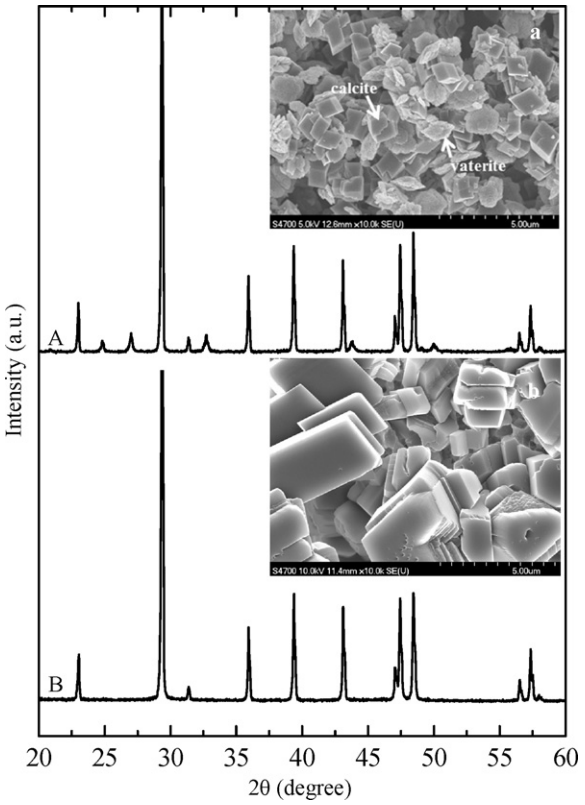

Fig. 7. XRD patterns and FE-SEM images of $CaCO_3$, after 30 min (A, a), and 60 min (B, b) by HAg-3.

surfaces of the vaterite particles [48]. The results described above indicate that HAg-1, HAg-2, and HAg-3 satisfy several criteria for green materials according to their purpose, reusability, and stability during storage. These materials are promising candidate catalysts for the hydration of CO_2 and its sequestration as $CaCO_3$.

4. Conclusions

HCA was immobilized onto silver nanoparticles that were confined within TAEA/TEPA/OAPS-functionalized mesoporous SBA-15. The surface charges of Ag/OAPS/SBA-15, Ag/TAEA/SBA-15, and Ag/TEPA/SBA-15 were found to be negative by zeta potential measurements. Thus, positively charged HCA was immobilized on the materials via electrostatic interactions. The biocatalytic activities of HAg-1, HAg-2, and HAg-3 were investigated by measuring the hydrolytic activity of the material toward p-NPA. The transformation of CO_2 to $CaCO_3$ was conducted over free as well as immobilized HCA. $CaCO_3$ formation was monitored by polarized light microscopy, and the CO_2 conversion efficiency was calculated using IC methods. Reusability studies of the nanosilver conjugated HCA indicated that the activity of the materials was ~25-fold higher than the activity of the free HCA for converting CO_2 to $CaCO_3$ even after 30 cycles. The amount of $CaCO_3$ precipitated over HAg-3 was higher than that precipitated over HAg-1 and HAg-2.

Acknowledgment

We acknowledge the financial support by grants from Korea CCS R&D Center funded by the Ministry of Education, Science and Technology of Korean Government.

References

[1] International Energy Outlook, Energy Information Administration, Department of energy, 2010, DoE/EIA-0484.
[2] G. Puxty, R. Rowland, A. Allport, Q. Yang, M. Bown, R. Burns, M. Maeder, M. Attalla, Environ. Sci. Technol. 43 (2009) 6427–6433.
[3] K.B. Lee, M.G. Beaver, H.S. Caram, S. Sircar, Ind. Eng. Chem. Res. 47 (2008) 8048–8062.
[4] D. Huang, O.V. Makhlynets, L.L. Tan, S.C. Lee, E.V. Rabak-Akimova, R.H. Holm, Proc. Natl. Acad. Sci. U.S.A. 108 (2011) 1222–1227.
[5] J.C. Hicks, J.D. Drese, D.J. Fauth, M.L. Gray, G. Qi, C.W. Jones, J. Am. Chem. Soc. 130 (2008) 2902–2903.
[6] A.L. Chaffee, G.P. Knowles, Z. Liang, J. Zhang, P. Xiao, P.A. Webley, J. Int. Greenhouse Gas Control 1 (2007) 11–18.
[7] A.R. Millward, O.M. Yaghi, J. Am. Chem. Soc. 127 (2005) 17998–17999.
[8] J.Y. Liang, W.N. Lipscomb, Biochemistry 27 (1988) 8676–8682.
[9] N.L. Rosi, C.A. Mirkin, Chem. Rev. 105 (2005) 1547–1562.
[10] C. Lei, Y. Shin, J. Lui, E.J. Ackerman, J. Am. Chem. Soc. 124 (2002) 11242–11243.
[11] A. Loidl-Stahlhofen, J. Schmitt, J. Noller, T. Hartmann, H. Brodowsky, W. Schmitt, J. Keldenich, Adv. Mater. 13 (2001) 1829–1834.
[12] W.T. Liu, J. Biosci. Bioeng. 102 (2006) 1–7.
[13] C. Guo, P. Boullanger, L. Jiang, T. Liu, Biosens. Bioelectron. 22 (2007) 1830–1834.
[14] D.A. Giljohann, D.S. Seferos, W.L. Daniel, M.D. Massich, P.C. Patel, C.A. Mirkin, Angew. Chem. Int. Ed. 49 (2010) 32803294.
[15] W. Anning, W. Hua, Z. Cheng, D.U. Zhiqiang, Z. Shemin, S. Shubao, Chin. J. Chem. Eng. 16 (2008) 612–619.
[16] F.N. Crespilho, R.M. Iost, S.A. Travain, O.N. Oliverira Jr., V. Zucolotto, Biosens. Bioelectron. 24 (2009) 3073–3077.
[17] N. Hashemifard, A. Mohsenifar, B. Ranjbar, A. Allamesh, A.S. Lotfi, B. Etemadikia, Anal. Chim. Acta 675 (2010) 181–184.
[18] M.S. Sadjadi, N. Farhadyar, K. Zare, Superlattices Microstruct. 46 (2009) 563–571.
[19] M.S. Sadjadi, N. Farhadyar, K. Zare, J. Nanosci. Nanotechnol. 9 (2009) 1365–1368.
[20] A.L. Crumbliss, S.C. Perine, J. Stonehuerner, K.R. Tubergen, J. Zhao, R.W. Henkens, O'Daly, Biotechnol. Bioeng. 40 (1992) 483–490.
[21] S. Phadtare, V.P. Vinod, K. Mukhopadhyay, A. Kumar, M. Rao, R.V. Chaudhari, M. Sastry, Biotechnol. Bioeng. 85 (2004) 629–637.
[22] K. Mukhopadhyay, S. Phadtare, V.P. Vinod, A. Kumar, M. Rao, R.V. Chaudhari, M. Sastry, Langmuir 19 (2003) 3858–3863.
[23] Y.Z. Chen, C.T. Yang, C.B. Ching, R. Xu, Langmuir 24 (2008) 8877–8884.
[24] B.J. Xin, S.F. Si, G.W. Xing, Chem-Asian J. 5 (2010) 1389–1394.
[25] F. Wang, C. Guo, L.R. Yang, C.Z. Liu, Bioresour. Technol. 101 (2010) 8931–8935.
[26] S. Bhattacharya, M. Schiavone, S. Chakrabarti, S. Bhattacharya, Biotechnol. Appl. Biochem. 38 (2003) 111–117.
[27] A.L. Crumbliss, K.L. McLachlan, J.P. Odaly, R.W. Henkens, Biotechnol. Bioeng. 31 (1988) 796–801.
[28] E. Ozdemir, Energy Fuels 23 (2009) 5725–5730.
[29] N. Liu, G.M. Bond, A. Abel, B.J. McPherson, J. Stringer, Fuel Process. Technol. 86 (2005) 1615–1625.
[30] F. Azari, M.N. Gorgani, Biotechnol. Bioeng. 62 (1999) 195–199.
[31] M. Vinoba, D.H. Kim, K.S. Lim, S.K. Jeong, S.W. Lee, M. Alagar, Energy Fuels 25 (2011) 438–445.
[32] M. Vinoba, K.S. Lim, S.K. Jeong, S.H. Lee, M. Alagar, Langmuir 27 (2011) 6227–6234.
[33] M. Vinoba, S.W. Jeong, M. Bhagiyalakshmi, M. Alagar, Bull. Korean Chem. Soc. 31 (2010) 3668–3674.
[34] M. Bhagiyalakshmi, R. Anuradha, S.D. Park, H.T. Jang, Micropor. Mesopor. Mater. 131 (2010) 265–273.
[35] M. Bhagiyalakshmi, L.J. Yun, R. Anuradha, H.T. Jang, J. Hazard. Mater. 175 (2010) 928–938.
[36] S.A. Madbouly, J.U. Otaigbe, A.K. Nanda, D.A. Wicks, Macromolecules 40 (2007) 4982–4991.
[37] K. De Witte, V. Meynen, M. Mertens, O.I. Lebedev, G. Van Tendeloo, A. Sepu lveda-Escribano, F. Rodrıĭguez-Reinoso, E.F. Vansant, P. Cool, Appl. Catal. B-Environ. 84 (2008) 125–132.
[38] C. Yu, J. Fan, B. Tian, D. Zhao, G.D. Stucky, Adv. Mater. 14 (2002) 1742–1745.
[39] W.S. Dodds, L.F. Stutzman, B. Sollami, J. Chem. Eng. Data 1 (1956) 92–95.
[40] J. Johnston, J. Am. Chem. Soc. 38 (1916) 975–1983.
[41] R. Tamaki, Y. Tanaka, M.Z. Asuncion, J. Choi, R.M. Laine, J. Am. Chem. Soc. 123 (2001) 12416–12417.
[42] Sujandi, E.A. Prasetyanto, S.C. Lee, S.E. Park, Micropor. Mesopor. Mater. 118 (2009) 134–142.
[43] V. Selvaraj, M. Alagar, J. Bionanosci. 2 (2008) 1–8.
[44] Y.J. Yao, K.S. Khoo, M.C.M. Chungb, S.F.Y. Li, J. Chromatogr. A 680 (1994) 431–435.
[45] A. Liljas, K.K. Kannan, P.C. Bergsten, I. Waara, K. Fridborg, B. Strandberg, U. Carlbom, L. Jarup, S. Lovgren, M. Petef, Nat. New Biol. 235 (1972) 131–137.
[46] M.M. Bradford, Anal. Biochem. 72 (1976) 248–254.
[47] P. Mirjafari, K. Asghari, N. Mahinpey, Ind. Eng. Chem. Res. 46 (2007) 921–926.
[48] R.G. Khalifah, J. Biol. Chem. 246 (1971) 2561–2573.
[49] N. Favre, M.L. Christ, A.C. Pierre, J. Mol. Catal. B: Enzym. 60 (2009) 163–170.
[50] D.L. Graf, Am. Miner. 46 (1961) 1283–1316.
[51] I. Sondi, J. Colloid Interface Sci. 234 (2001) 208–214.